Boosting total oxidation of methane over NiO nanocrystalline decorated ZnO-CoNi solid solution via photothermal synergism

Chen Sun [a,b,1], Kunfeng Zhao [a,*,1], Adam Boies [c], Shuning Xiao [b], Zhiguo Yi [a,b,**]

[a] State Key Lab of High Performance Ceramics and Superfine Microstructure, Shanghai Institute of Ceramics, Chinese Academy of Sciences, Shanghai 201899, China
[b] School of Materials and Chemistry, University of Shanghai for Science and Technology, Shanghai 200093, China
[c] Department of Engineering, University of Cambridge, Cambridge CB21PZ, UK

ABSTRACT

In the context of global warming and atmospheric methane growth, photo-assisted total oxidation of methane is of great importance to diminish greenhouse effect. However, catalytic oxidation of methane at ambient conditions remains a formidable challenge because of its high structure stability. Herein, we report a highly active and stable NiO nanocrystalline decorated on ZnO-CoNi solid solution (NiO/ZnO-CoNi) catalyst which enables 88 % photocatalytic conversion of methane to CO_2 and H_2O under ambient conditions to maintain a continuous reaction. The unprecedented photocatalytic performance of NiO/ZnO-CoNi originates from the high mobility of surface lattice oxygen of supported NiO nanocrystallines driven by the photogenerated electrons and internal electric field of ZnO-CoNi solid solution. More importantly, the methane conversion of NiO/ZnO-CoNi remains higher than 37 % even when the methane concentration is up to 5000 ppm, showing promise for methane elimination applications in the vicinity of large methane emission sources.

1. Introduction

Global warming, caused by excessive greenhouse gas emissions, is posing a serious threat to the survival of life on earth includes human beings. The methane contributes roughly one-third of the 1.2 °C of global temperature rise since preindustrial [1]. The climatic impacts of methane are increasing due to the rapid growth of atmospheric level of methane, despite the decrease in anthropogenic emissions the latest few years during the COVID-19 pandemic lockdown [1,2]. The increasing wetland emissions and reducing atmospheric sinks account for the acceleration in methane growth rate [1–3]. As a result, methane removal from atmosphere is an acute need, in addition to reducing methane emissions during fossil-fuel extraction, to achieve the goal of Paris Agreement.

Convert methane into value-added chemicals like methanol, formaldehyde, acetylene and other hydrocarbon compounds [4–8] is an ideal choice. However, the concentration of atmospheric methane is only 1900 ppb [3] and the energy requirement to break the C-H bond of methane is up to 434 kJ mol^{-1} [9]. The significant energy required for atmospheric methane capture and conversion implies that it is unrealistic to produce value-added chemicals from low concentration sources, such as atmospheric methane. A more viable pathway is to oxidize methane to CO_2 and H_2O by photocatalysts at ambient temperature without capture [10–12]. And the greenhouse effect of CH_4 is as high as 84 times of that of CO_2 in 20 years [1]. Thus, the conversion of atmospheric CH_4 to CO_2 (total oxidation of methane, TOM) is of great importance to slow global warming.

In our previous work [10,12], ZnO exhibited a much higher catalytic activity than commercial P25 in the TOM reaction under simulated sunlight irradiation, and the introduction of a small amount of CuO and Ag further improved the activity. The polar structure of ZnO, electron sink and photo-sensitizer effect of compact combination CuO and Ag contribute to the unexpected activity. Integrating these photocatalysts with Solar Chimney Power Plants were considered to have great potential to counter global warming [13]. The acute challenge is that relatively low reaction rate of photocatalysis and huge volume of atmosphere result in a considerable difficult and large-scale project needed for atmospheric methane removal.

The removal technology of high concentration of methane at ambient temperature may focus conversion technologies in the vicinity of large emission sources of methane, such as wetlands, fossil-fuel extraction, landfills to achieve significant emission reductions. Thermal catalysis can have high reaction rates, providing possible directions for improvement of photocatalysis, although temperatures higher than 300 °C often required for activation of C-H bond of methane molecule [14,15]. Feng et al [16]. demonstrated that, under the photothermal synergistic condition, $PdO/Mn_3O_4/CeO_2$ on halloysite nanotubes could realize efficient conversion of 0.5 % CH_4 and the light-off temperature of TOM was reduced sharply from 265 to 180 °C. Kang et al [17]. designed a Pt/TiO_2-WO_3 catalyst which achieved a 70 % photothermal catalytic conversion of 1 % C_3H_8 to CO_2 at 90 °C.

In this study, Co and Ni with good catalytic activity in alkane oxidation [18,19] were chosen to synergize with polarized ZnO. The optimized NiO/ZnO-CoNi shows excellent photocatalytic activity under ambient conditions. Its methane conversions of TOM are 88 % and 37 % for 100 and 5000 ppm methane in a continuous reaction mode, respectively. The good redox property of NiO/ZnO-CoNi catalyst at ambient temperature under irradiation is responsible for its high activity.

2. Experimental section

2.1. Materials

Zinc nitrate hexahydrate ($Zn(NO_3)_2 \cdot 6H_2O$), Cobalt(II) nitrate hexahydrate ($Co(NO_3)_2 \cdot 6H_2O$, Nickel(II) chloride hexahydrate ($NiCl_2 \cdot 6H_2O$) and oxalic acid dihydrate ($H_2C_2O_4 \cdot 2H_2O$), were purchased from Sinopharm Chemical Reagent Co., Ltd. (Shanghai, China). All these chemicals were used as received without further purification.

2.2. Samples preparation

The catalysts were synthesized by coprecipitation method: Firstly, a mixture of 0.015 moles of $Zn(NO_3)_2 \cdot 6H_2O$, $Co(NO_3)_2 \cdot 6H_2O$, $NiCl_2 \cdot 6H_2O$, and 0.015 moles of $H_2C_2O_4 \cdot 2H_2O$ were dissolved in 100 mL of deionized water, respectively. Then, oxalic acid solution was added drop-wise to the mixed solution of metal ions under stirring. After reaction for 2 h, the obtained precipitates were separated from the liquid by filtration and rinsed several times with deionized water. After that, the resulted precipitates were dried at 60 °C for 8 h, calcined at 350 °C in air for 6 h and reduced at 250 °C in 5 % H_2/Ar for 2 h. The catalysts were noted as ZnO-CoNi(x:y) where x:y represented the atomic ratio of n(Zn)/n(Co+Ni). Unless otherwise specified, the molar ratio of Co to Ni is 1:3. For comparison, the ZnO, ZnO-Co, and ZnO-Ni were also prepared by the same method.

2.3. Characterizations

The morphologies of samples were observed by scanning electron microscope (SEM, ZEISS Sigma 300, Germany) and high angle ring dark field scanning transmission electron microscope (HAADF-TEM, EM-ARM300F, Japan). The Brunauer-Emmett-Teller (BET) specific surface areas of the samples were measured by a specific surface area analyzer (Micromeritics ASAP 2460, USA) at −196 °C. The crystalline phases of ZnO-CoNi samples were analyzed using high-resolution X-ray diffractometer (XRD, Bruker D8 ADVANCE, Germany) with Cu-Kα (λ = 0.15418 nm) radiation. Raman spectrometer (Horiba LabRAM HR Evolution, Japan) and micro-area energy-dispersive X-ray spectroscopy (EDS) equipped on HAADF-TEM were used to identify local structure and elemental distribution. The PerkinElmer Lambda 900 UV-Vis-NIR spectrometer (USA) equipped with integrating spheres covered with $BaSO_4$ as reference was used to measure light absorption and further calculate the band gap. The chemical states of ZnO-CoNi composites were investigated by X-ray photoelectron spectroscopy (XPS, Thermo

Scientific K-Alpha, USA) equipped with monochromated Al Kα radiation. In situ DRIFTS experiment was performed with Fourier Transform Infrared Spectrometer (Thermo Fisher Scientific Nicolet iS50R, USA). The sample cell has an extra quartz window to enable signal collection under irradiation. The background was recorded in N_2. Then CH_4, CH_4 +O_2, and O_2 with a flow rate of 30 mL min⁻¹ was introduced sequentially, and the corresponding spectra were collected automatically. In situ H_2-TPR was performed in the same sample cell. The 30 mg sample was heated from 50 °C to 500 °C in 5 % H_2/Ar at a heating rate of 5 °C min⁻¹ and a flow rate of 30 mL min⁻¹. The H_2 signal was monitored on line with a thermal conductivity detector. Prior to DRIFTS and H_2-TPR test, 30 mg sample was pretreated in 5 % H_2/Ar at 250 °C for 2 h to remove surface contaminants.

2.4. Photocatalytic total oxidation of methane

The photocatalytic total oxidation of methane was carried out at a continuous flow mode on a photothermal synergistic micro reaction system CEL-GPPCT (Beijing China Education Au-light Co., Ltd). Typically, 0.2 g of photocatalysts in powder form (0.2–0.4 mm) were filled at the bed of quartz tube reactor, 6 mm in inner diameter and 500 mm in height. Then the feed gas (100 ppm CH_4, 21.1 % O_2 balanced by N_2) was passed through the sample at a flow rate of 25 mL min⁻¹ with corresponding gas hourly space velocity (GHSV) of 7500 mL g_{cat}^{-1} h⁻¹. Instantly, the samples were irradiated by a 300 W Xe lamp (CEL-PF300-T8) with ~1200 mW cm⁻² intensity on their surface. The irradiation area was 1.1 cm². The effluent gas was analyzed by a gas chromatograph (GC-7920, Beijing China Education Au-light Co., Ltd) equipped with flame ionization detector (FID) and methanizer to detect organic molecules (CH_4 etc.), CO and CO_2. The kinetic data was measured in 5000 ppm CH_4 to control a relative low CH_4 conversion and to remove the impact of thermal effect and diffusion.

3. Results and discussion

3.1. The TOM photocatalytic performances of ZnO-CoNi catalysts

The performances of ZnO doped with different ratios of Co, Ni and CoNi for photocatalytic TOM were tested firstly at 7500 mL g_{cat}^{-1} h⁻¹ of GHSV, 100 ppm of CH_4, 1200 mW cm⁻² light intensity and ambient condition, in order to verify the synergy among Co, Ni and ZnO. It can be seen in Fig. 1a, for pure ZnO, CH_4 conversion is only 25 %. After Co and Ni doping, the activity varies with Zn/metal proportion and presents as a volcano curve with the highest activity at 66 % and 54 % for ZnO-Ni (10:5) and ZnO-Co(9:6), respectively (Fig. S1a). In the case of CoNi co-doping, the activity increases further indicating there is a synergetic effect between Co and Ni. The Co/Ni ratio and doping amount have a directly effect on the activities of ZnO-CoNi catalysts, and the optimized component of ZnO-CoNi is 1:3 of Co/Ni ratio (Fig. S1b) and 9:6 of ZnO/ CoNi ratio (Fig. S1a). The CH_4 conversion of the optimized ZnO-CoNi (9:6) is dramatically increased to 88 %, almost 4 times of that of pure ZnO (Fig. 1a). Obviously, both Co and Ni doping can promote activity of ZnO, and appropriate proportion of co-doping results in a further promotion. Notably, ZnO-CoNi(9:6) is much more active than the Ag/ZnO we reported previously [10], under the same reaction conditions (Fig. S1a). In addition, ZnO-CoNi(9:6) possesses good reaction and cycling stability without visible deactivation during 20 h test and repeatedly light turn off and on (Fig. 1). The TOM was identified from the chromatogram spectra where CO_2 was the only detected product (Fig. S2). The good activity and stability of ZnO-CoNi(9:6) indicate the catalyst a promising application prospect.

The flow rate and CH_4 concentration directly affect the reaction rate of catalysts which are important parameters in application. As shown in Fig. 2a and b, CH_4 conversion of ZnO-CoNi(9:6) shows different degrees of decline with the gas flow rate and CH_4 concentration increasing. The CH_4 conversion of ZnO-CoNi(9:6) at 100 ppm and 100 mL min⁻¹ is 51
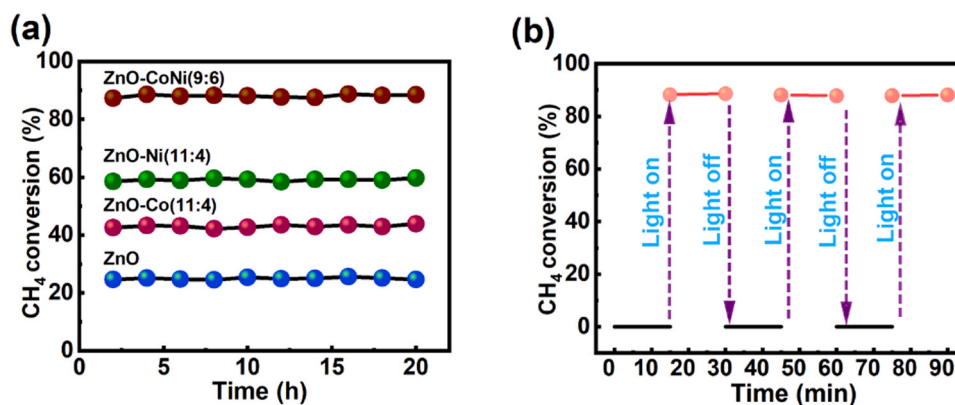
Fig. 1. (a) Photocatalytic activities and durabilities of ZnO, ZnO-Co(11:4), ZnO-Ni(11:4) and the optimized ZnO-CoNi(9:6). (b) Effect of illumination on activity of ZnO-CoNi(9:6). (Reaction conditions: 100 ppm CH_4, 21.1 % O_2, bal. N_2, 0.2 g of catalyst, 25 mL min^{-1} of flow rate).
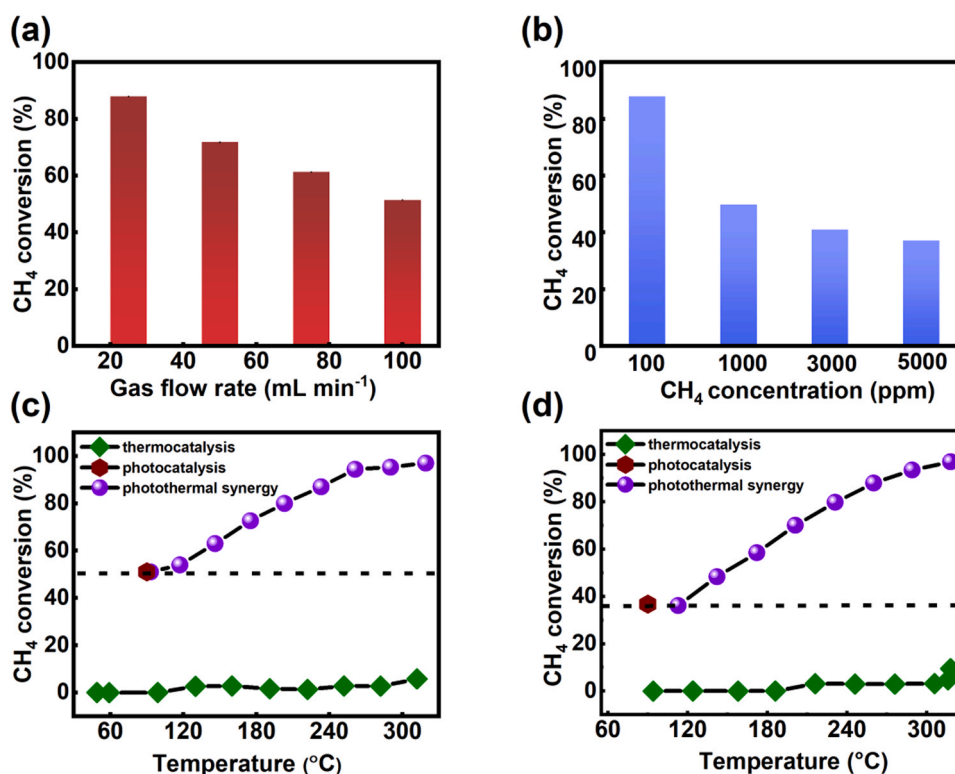

Fig. 2. Methane conversion of ZnO-CoNi(9:6) under various conditions: (a)100 ppm methane and full arc irradiation at different flow rates; (b) different methane concentrations at 25 mL min^{-1} flow rate and full arc irradiation; (c) 100 ppm methane and 100 mL min^{-1} with different catalytic modes (thermo-, photo- and photothermal catalysis); (d) 5000 ppm methane and 25 mL min^{-1} with different catalytic modes.

%, while at 5000 ppm and 25 mL min^{-1} it is 37 %. The relatively high conversions at high flow rate and high concentration indicate ZnO-CoNi (9:6) possesses a high CH_4 conversion rate under photocatalytic condition, which indicates its viability for wider use.

The temperature of catalyst bed rapidly rises to about 90 °C under full arc irradiation and remained the temperature during the whole reaction period. To clarify the contributions of light and heat, TOM reactions at high flow rate (Fig. 2c) and high concentration (Fig. 2d) were performed under light, heat, and photothermal synergy conditions, respectively. It can be seen that, without irradiation, there is almost no CO_2 generated even when the temperature increases to above 300 °C, and the methane conversion is lower than 10 %. On the contrary, under irradiation, the photocatalytic activity of methane increases significantly with the increase of temperature. All of the methane is converted to CO_2 when the temperature rises to about 280 °C.

In order to obtain the intrinsic influence of light and heat on the photothermal catalytic activity, the specific rates per catalyst mass and apparent activation energy (E_a) were measured (Table S1 and Fig. S3). The specific rate of ZnO-CoNi(9:6), contributed by individual photocatalysis, is 1935 μmol g^{-1} h^{-1} at GHSV of 30000 mL g^{-1} h^{-1} which dramatically increases to 3536 and 4688 μmol g^{-1} h^{-1} at 180 and 270 °C under photothermal synergy condition, respectively. The photothermal specific rate of ZnO-CoNi(9:6) is 4 times of that of PdO/ Mn_3O_4/CeO_2 (938 μmol g^{-1} h^{-1}) at 180 °C under similar conditions [16]. Although, it becomes lower than PdO/Mn_3O_4/CeO_2 (4688 vs 6844 μmol g^{-1} h^{-1}) when temperature rises to 270 °C, ZnO-CoNi(9:6) is still much active than non-noble metal catalyst with specific rate 360 times higher that of ZnO/$La_{0.8}Sr_{0.2}CoO_3$ (13 μmol g^{-1} h^{-1}) [20]. However, the specific rates of ZnO-CoNi(9:6) contributed by heat are only 39 and 100 μmol g^{-1} h^{-1} at 180 and 270 °C, respectively. The specific rate of

ZnO-CoNi(9:6) in photothermal condition is much higher than the sum of those in individual heat or light. The E_a obtained from the Arrhenius equation (Table S1 and Fig. S3) is greatly reduced from 64.8 to 5.7 kJ mol^{-1} implying a photothermal synergism. Generally, the catalytic TOM reaction on ZnO-CoNi(9:6) catalyst is a photodriven process. Thermal energy can significantly improve the photocatalytic activity of TOM, although itself can hardly activate methane at temperature lower than 300 °C.

3.2. Physical and chemical properties of ZnO-CoNi catalysts

The morphologies and structures of pure and doped ZnO were investigated to understand the origin of the excellent performances of ZnO-CoNi(9:6). As shown in Fig. S4, the SEM images of pure ZnO, ZnO-Co(11:4), ZnO-Ni(11:4) and ZnO-CoNi(9:6) samples show an irregular blocky morphology with the size of 2–6 μm assembled from nanosheets. Apparently, doping of Co and/or Ni decreases the particle size resulting in an increase of specific surface area of doped ZnO. The BET specific surface areas of pure ZnO, ZnO-Co(11:4), ZnO-Ni(11:4) and ZnO-CoNi (9:6) nanopowders are 28, 41, 42 and 62 m^2 g^{-1} (Table S2), respectively.

The XRD patterns of samples are shown in Figs. 3a and S5. All samples present a typical wurtzite structure type as pure ZnO (JCPDS No. 99–0111). The crystalline size of ZnO and doped ZnO, calculated by the Scherrer equation, decreases from 17.8 nm for pure ZnO to 9.9 nm for ZnO-CoNi(10:5) first, and then increases to 18.6 nm for ZnO-CoNi (8:7). Meanwhile, for ZnO-Ni(11:4) and ZnO-CoNi with the ratio of n (Zn)/(n(Co)+n(Ni)) $\leq$ 12:3, a new diffraction peak centered at 43° emerges which can be ascribed to NiO (JCPDS No. 44–1159) and its intensity becomes stronger with the increase of Ni content, indicating more NiO nanocrystallines decorated on the surface of ZnO. The crystalline size of NiO calculated by the Scherrer equation increases from 6.1 nm for ZnO-CoNi(12:3) to 6.9 nm for ZnO-CoNi(8:7). And the crystalline size of NiO on ZnO-Ni(11:4) is 6.6 nm, similar to that of ZnO-CoNi(9:6). However, there is no observable Co segregation for ZnO-CoNi and ZnO-Co(11:4) samples.

The enlarged XRD (Fig. S6) shows that, for Co, Ni, CoNi doped samples, the diffraction peaks of ZnO shift to high angle, indicating lattice contraction of doped ZnO due to the substitution of tetra-coordinated Zn^{2+} (0.60 Å) by the smaller Co^{2+} (0.58 Å) and Ni^{2+} (0.54 Å) and the formation of ZnO-Co, ZnO-Ni and ZnO-CoNi solid solution [21]. The XRD analysis in Table S2 shows that pure ZnO has P63mc space group lattice parameters of a = 3.248 Å and c = 5.213 Å. It can be seen that doping has a negligible effect on the parameter of a, while the parameter of c decreases in different degrees after Co/Ni doping. Although with a smaller ionic radius, ZnO-Ni(11:4) has a comparable c with ZnO-Co(11:4) (5.204 vs 5.203 Å), that is because besides merged in ZnO lattice, part of Ni decorated on the surface in the form of

NiO (Fig. S6b). As for ZnO-CoNi samples, parameters of c decreases to 5.189 Å for ZnO-CoNi(11:4) with increasing Co and Ni content. This value is smaller than that of ZnO-Ni(11:4) and ZnO-Co(11:4), probably because the solubility of Ni increased as Co and Ni codoping. Higher CoNi concentration does not cause further alterations, and the lattice parameters remain nearly invariable even for ZnO-CoNi(8:7), indicating that it has an upper limit for Co^{2+} and Ni^{2+} dissolution into the ZnO lattice.

Raman spectroscopy is a more sensitive technology for trace impurities and amorphous substances. The Raman spectra of ZnO-CoNi samples with the ratio of n(Zn)/(n(Co)+n(Ni)) from 12:3–7:8 are shown in Fig. 3b. The typical Raman spectrum of wurtzite ZnO has six Raman-active modes at 99, 378, 410, 438, 574 and 590 cm^{-1}, two strong peaks of which centered at 99 and 438 cm^{-1} correspond to the E$_{2L}$ and E$_{2H}$ modes, respectively [22]. However, in Fig. 3b, all ZnO-CoNi samples show similar spectra but they are quite different compared to wurtzite ZnO. The Raman spectra of the samples show a weaken peak at 430 cm^{-1} and addition new peaks at 535, 674 and 1101 cm^{-1}. The weakening of peak at 430 cm^{-1} and newly peak at 674 cm^{-1} in ZnO-CoNi samples are due to the structural defects and Zn-O disorder induced by dopants [22,23]. The remarkable 535 cm^{-1} band can be assigned to the overlap of local vibrations of Co/Ni coupled with donor defects such as doubly occupied oxygen vacancies and zinc interstitials [24,25] and Zn-O disorder [22]. The peak at 1101 cm^{-1} belongs to the Ni-O stretching mode of NiO [18]. Simply, all Raman peaks, except 1101 cm^{-1}, are mainly caused by the defects and disorder of ZnO-CoNi solid solution induced by Co and Ni doping. NiO nanocrystalline presents on all doped ZnO samples from the peak at 1101 cm^{-1} in their Raman spectra, and, there is no Raman peak belongs to cobalt oxides, showing consistency with XRD. Combined the Raman and XRD results, the structure of ZnO-CoNi can be deduced to be NiO nanocrystalline decorated on ZnO-CoNi solid solution.

The HAADF-STEM images of ZnO-CoNi(9:6) are shown in Fig. 4 to give an observable characterization of the microstructure of ZnO-CoNi. Fig. 4a shows that ZnO-CoNi(9:6) has an irregular blocky structure as that shown in SEM (Fig. S4). The magnified STEM (Fig. 4b and c) images reveal that ZnO-CoNi(9:6) nanosheets are stacked by nanoparticles with diameter of 5–10 nm. Element mapping analysis (Fig. 4d-g) shows that the distribution of Zn, Co, Ni and O elements is relatively uniform in most region, except for the high density of Ni in circled part which confirming the existence of NiO nanocrystalline. The HAADF-STEM further indicates that NiO nanocrystalline is segregated and decorated on ZnO-CoNi solid solution.

The UV-Vis spectra of ZnO, ZnO-Co and ZnO-Ni are shown in Fig. S7. It can be seen that after Co doping, the band gap decreases from 3.24 eV for pure ZnO to 2.61 eV for ZnO-Co(13:2) and 2.35 eV for ZnO-Co(11:4) respectively, which is a directly evidence of enhanced visible light absorption capacity. Combining with XRD results (Table S2), the increase
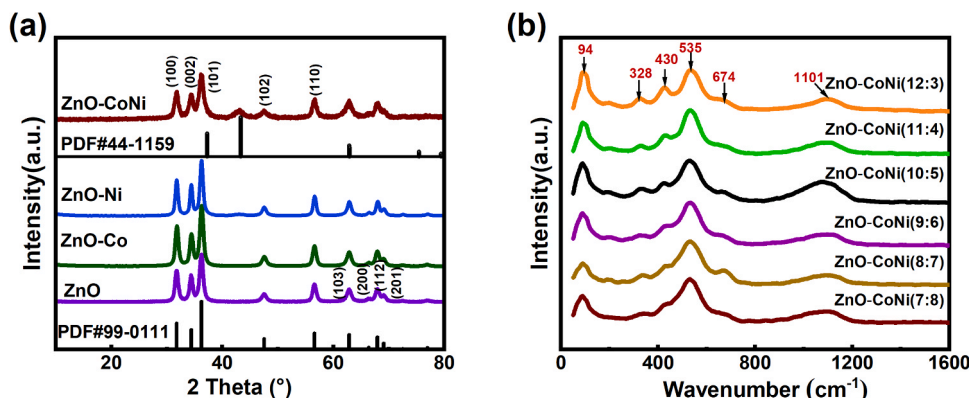

Fig. 3. (a)XRD patterns of pure ZnO, ZnO-Co(11:4), ZnO-Ni(11:4) and ZnO-CoNi(9:6), (b) Raman spectra of ZnO-CoNi with different CoNi ratios.
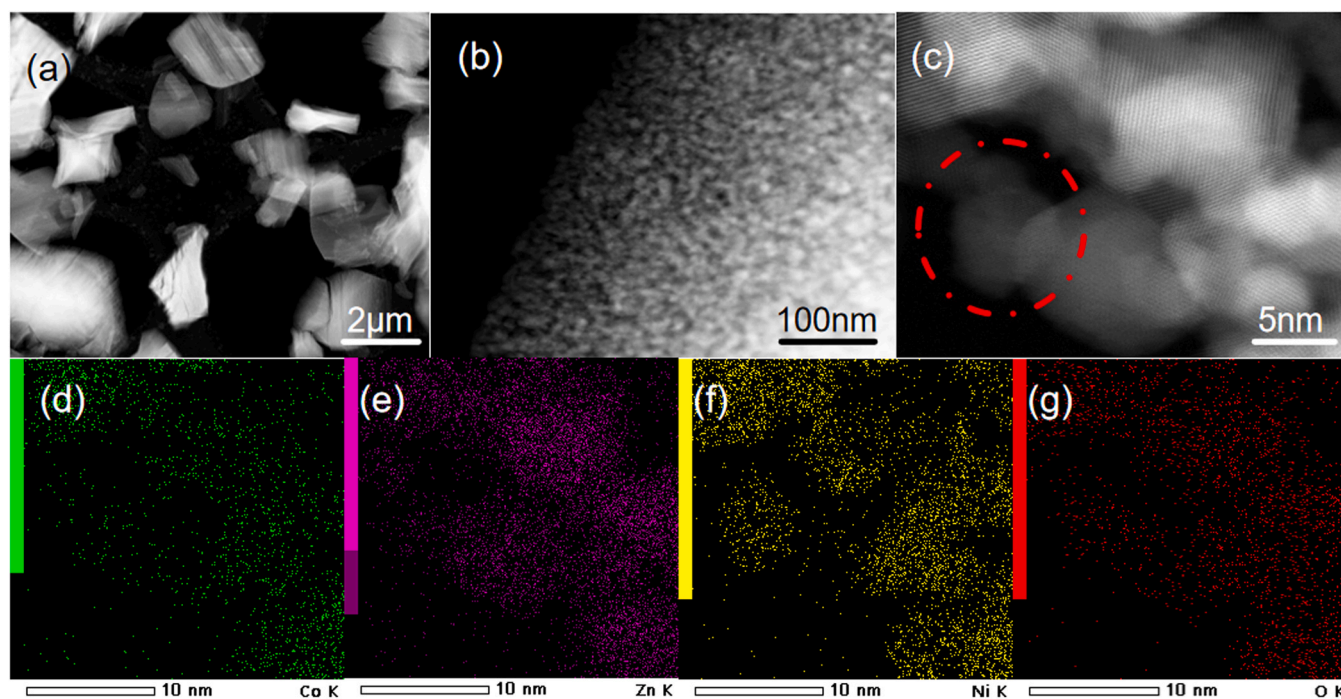
Fig. 4. The HAADF-STEM images of ZnO-CoNi(9:6) (a-c) and corresponding EDS mapping of Zn, Co, Ni and O (d-g).

of visible light absorption due to formation of ZnO-Co solid solution. While the band gap of ZnO-Ni(13:2) and ZnO-Ni(11:4) are 3.15 and 3.06 eV, which are very close to that of ZnO. That is because the solubility of Ni in ZnO lattice is low and part of Ni exists as NiO

nanocrystallines on ZnO-Ni solid solution (Fig. S6b). For ZnO-CoNi samples, the band gap can even be reduced to 1.85 eV (Fig. S8, ZnO-CoNi(8:7)) due to more substitution of Ni ions consistent with XRD results. The specific structure of ZnO-CoNi(9:6) results in a narrower band
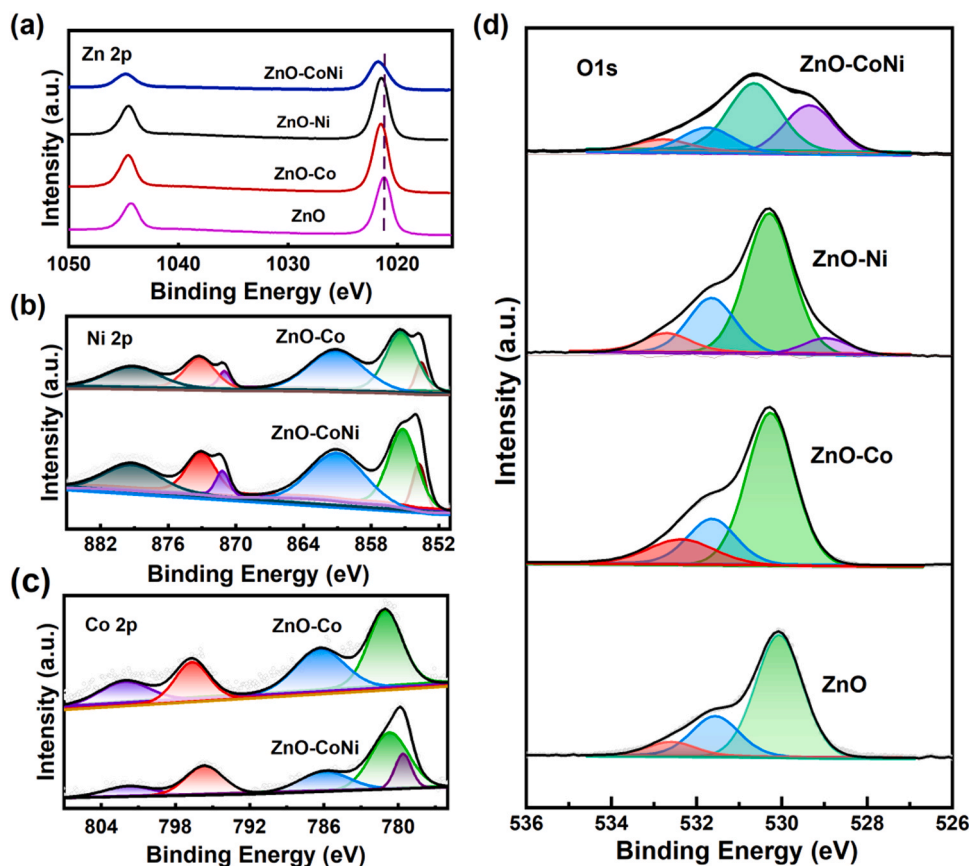

Fig. 5. XPS spectra of Zn2p (a), Ni2p (b), Co2p (c), and O1s (d) for pure ZnO, ZnO-Co(11:4), ZnO-Ni(11:4) and ZnO-CoNi(9:6).

gap (2.15 eV) and a stronger visible light absorption capacity compared with pure ZnO (Fig. S7 and S8) which are usually beneficial for photocatalysis.

XPS analyses were performed in order to determine the doping induced changes of surface chemical properties of catalysts. The spectra and quantification results are shown in Fig. 5a-d and Table S3. As can be seen from Fig. 5a, for pure ZnO, the binding energy of Zn $2p_{3/2}$ is at 1021.2 eV, and it shifts to higher energy (1021.5, 1021.5 and 1021.8 eV) after the Co, Ni doping and CoNi co-doping. The positive energy shifts indicate that Zn ions as electrons donor or holes receptor [26].

For Ni containing catalysts, ZnO-Ni(11:4) and ZnO-CoNi(9:6), there are three doublet peaks centered at ~853.6, 855.4 and 861.1 eV (Fig. 5b), which are ascribed to Ni^{2+}, Ni^{2+} with holes, and satellite peak, respectively [27–29]. The Co containing catalysts, ZnO-Co (11:4) and ZnO-CoNi, have similar peaks at binding energy of ~781.0 and 786.3 eV which are peak feature of $2p_{3/2}$ of Co^{2+} and its shake-up satellite [30,31] (Fig. 5c). It is particularly noteworthy that the single peak at 779.6 eV is due to the Auger electron peak of Ni $L_3M_{23}M_{23}$ and $L_2M_{23}M_{23}$ other than the photoelectron peak of Co when using Al Kα radiation as the excitation source [32,33]. According to the peak-fitting (Fig. 5b and c) and quantification results of Table S3, the doped Co and Ni are Co^{2+} and Ni^{2+} in all of the catalysts.

The O species of all catalysts are composed of surface lattice oxygen (O_{latt}), adsorbed oxygen (O_{ads}), and surface hydroxyl groups (O_{OH-}) at $\leq$ 530.6 eV, ~531.6 eV and ~ 532.6 eV, respectively (Fig. 5d). It is noteworthy that when Ni is doped, small amount of lattice oxygen species at lower binding energy are detected. The amount of it increased to 33 % when Co is co-doped (Fig. 5d and Table S3). According to the XRD, Raman and HAADF-STEM results, the lattice oxygen species at lower binding energy might originate from the small nanocrystallines of NiO segregated from ZnO-CoNi solid solution. The low binding energy of lattice O^{2-} indicates NiO might be an electrons receptor. In addition, lattice oxygen with low binding energy generally means high lattice

oxygen mobility, which is also considered to be an important factor for activity increasing in thermal catalysis [34].

3.3. TOM reaction mechanism on ZnO-CoNi

In order to reveal the reaction mechanism of photocatalytic TOM, in situ DRIFTS experiments on the catalyst ZnO-CoNi(9:6) were performed. From Fig. 6, the characteristic bands of CH_x (asymmetric peak centered at ~1339 cm^{-1}) and intermediates (around ~1500 cm^{-1}) are appeared simultaneously with methane gas (1305 cm^{-1} and 3015 cm^{-1}) [35] after introduction of CH_4. This indicates that ZnO-CoNi(9:6) can activate methane to generate CH_x, and further convert to intermediates by reacting with reactive oxygen species on the catalyst surface. This process can be accelerated by light or heat, since intensities of CH_x and intermediates increased after light on or heated (Fig. 6b and c vs a). Accordingly, chemisorbed H_2O is simultaneously produced and its peak at ~3673 cm^{-1} [35] can be observed under light or 180 °C in the dark conditions. The low content of chemisorbed H_2O produced at 25 °C in the dark might be the reason for the absence of peak at ~3673 cm^{-1}. However, the peak of gas-phase CO_2 (2309 and 2370 cm^{-1}) [36] can be observed only under light condition during CH_4, O_2 co-introduced, and the spectral intensity at 180 °C is much higher than that at 25 °C (Fig. 6b and d). This observation proves that methane can be totally oxidized to CO_2 and H_2O on ZnO-CoNi(9:6) catalyst with the assistant of light, and thermal energy accelerates the reaction rate, which is consistent with the activity test (Fig. 2).

The distinct performance of ZnO-CoNi(9:6) under irradiation may due to the different intermediate species from that in the dark. As shown in Fig. 6, the intermediates can be attributed to formate (1580 [36], 1606 cm^{-1} [37], monodentate formate; ~1470 cm^{-1}, bidentate formate [37]) and carbonate species (~1325 [11], ~1516 cm^{-1} [35], carbonate). Without irradiation, the intermediates on ZnO-CoNi are bidentate and monodentate formate (1470 and 1580 cm^{-1}, Fig. 6a) and carbonate species (1325, 1516 cm^{-1}, Fig. 6c) at 25 and 180 °C, respectively. Both
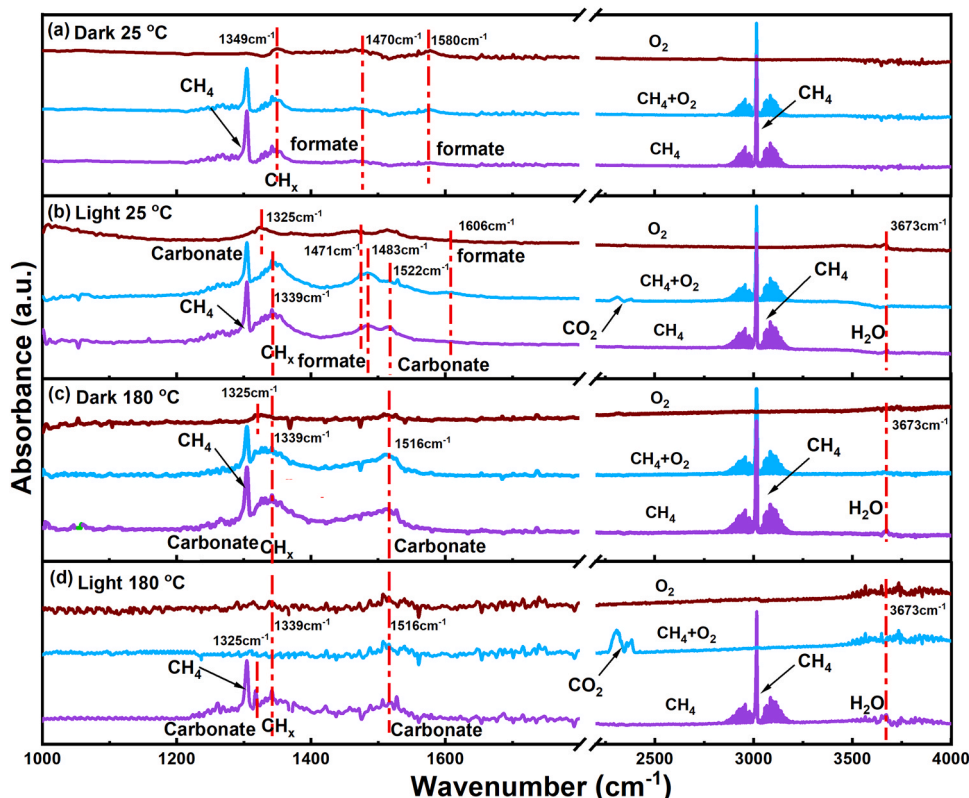

Fig. 6. In situ DRIFTS measurement on ZnO-CoNi(9:6) catalyst under various conditions.

of them cannot be converted to CO_2 by O_2 in the dark when the temperature is lower than 180 °C. Under irradiation at 25 °C, the remarkable signals of bidentate formates (1471, 1483 cm^{-1}) and relatively weak signals of carbonates (1325, 1522 cm^{-1}) are appeared (Fig. 6b). The intensity of bidentate formates increase further and monodentate formates (1606 cm^{-1}) are appeared when CH_4 is replaced by $CH_4 + O_2$. This suggests that more bidentate formates are produced in $CH_4 + O_2$ flow, and the repulsion among the bidentate formates at high concentration resulted the transition of bidentate formates to monodentate formates prior to decomposition [36]. In the following oxygen purging process, the bands of formates disappear while that of carbonates remain unchanged. When increasing the temperature to 180 °C under irradiation, the carbonates (1516 cm^{-1}) are detected and remained without decomposition even in pure O_2 flow just like the situation in light-only condition (Fig. 6d). However, there is no visible formates both under CH_4 and $CH_4 + O_2$ atmosphere, which is mainly due to the fast decomposition rate of formates under photothermal conditions. The results suggest that formates especially monodentate formates are key intermediates for TOM at low temperature. Light promotes the reaction of CH_x and reactive oxygen to form high concentration of bidentate formates and following evolution to monodentate formates which are more easily to decompose to CO_2 and H_2O, and then TOM reaction occurred. While heat further accelerates the rate of TOM by speeding up the decomposition of formates.

The in situ H_2-TPR was conducted to determine the origin of the reactive oxygen. As shown in Fig. 7a, there is almost no reduction peak for ZnO in the temperature range of 25–480 °C, regardless of the presence or absence of light irradiation. For ZnO-CoNi(9:6), the H_2 consumption signal can be clearly seen at 386 °C which is ascribed to the reduction of NiO on ZnO-CoNi solid solution [18] in the dark. Unexpectedly, for ZnO-CoNi(9:6), the reduction temperature decreased dramatically to 345, 251 and even to only 40 °C after light irradiation. From Fig. 7b, ZnO-Co(11:4) shows three weak reduction peaks centered at 192, 288 and 404 °C, while ZnO-Ni(11:4) shows a continuous reduction peak range from 40 to 140 °C, and a large peak centered at 380 °C under irradiation. According to the normalized integral areas of reduction peaks (Table S4), the total areas of reduction peaks of ZnO-Ni (11:4) and ZnO-CoNi(9:6) are 96 and 100, while that of ZnO-Co(11:4) is only 5 %. The result indicates that almost all of the H_2 consumptions originate from NiO reduction. The reduction at low temperature can be ascribed to the photo-assisted reduction of small NiO nanocrystallines and that at high temperatures might related to the reduction of large NiO particles. Although ZnO-Co solid solution is redox inert like pure ZnO. However, Co doping can promote NiO photo-assisted reduction, the H_2 consumptions peaks area of ZnO-CoNi(9:6) at temperature below 140 °C is 31 which is 4 times of that of ZnO-Ni(11:4), and the reduction temperatures shift to lower temperature (40 °C vs 51–122 °C; 345 °C vs 380 °C).

Comprehensive with the UV-Vis (Fig. S7 and S8) and XPS (Fig. 5), the H_2 consumption at 40 °C is mainly be due to the synergy of photoexcitation and the surface lattice O^{2-} of NiO nanocrystalline with low binding energy. Under light irradiation, the photogenerated electrons and holes are induced by the excitation of ZnO-CoNi(9:6), the photogenerated holes transfer to the surface of ZnO-CoNi solid solution and oxidize H_2 to H^+, the generated H^+ cations migrate to the supported NiO nanocrystallines and react with the lattice O^{2-} with low binding energy to form H_2O, the photogenerated electrons transfer to NiO and combine with Ni^{2+} to form Ni^0 and complete the reduction of NiO.

Based on the above results, the mechanisms of TOM on ZnO-CoNi catalyst are proposed. The microstructure of ZnO-CoNi catalyst is NiO nanocrystalline decorated on ZnO-CoNi solid solution determined by XRD (Fig. 3a, Table S2), Raman (Fig. 3b) and HAADF-STEM (Fig. 4). The NiO nanocrystallines are the active sites for TOM reaction proceeding and the photoexcited ZnO-CoNi solid solution promotes the generation and decomposition of formate intermediate species, thus accelerates the TOM reaction rates.

As shown in Fig. 8, for thermocatalysis, only small amount of methane can be activated by surface lattice oxygen of NiO nanocrystallines and converted to formates and carbonates at low and high temperatures, respectively. The low mobility of surface lattice oxygen of NiO nanocrystallines (Fig. 7) results in a high affinity between ZnO-CoNi and formates or carbonates (Fig. 6a and c). The adsorbed formates or carbonates species poison ZnO-CoNi catalyst and hinder the TOM reaction. The light irradiation over the ZnO-CoNi catalyst brings a great change in TOM route. Firstly, a large amount of photogenerated electrons and holes are excited and spatially separated to NiO and ZnO-CoNi solid solution surface due to the narrow band gap and internal electric field of ZnO-CoNi (Fig. S8). Secondly, the CH_4 molecules are activated by the photogenerated holes at the surface of ZnO-CoNi to form CH_x (Fig. 6). Thirdly, the resulted CH_x species transfer to NiO and react with the low binding energy O^{2-} of NiO to form high concentration of bidentate formates and transform to weakly adsorbed monodentate formates which further degrade to CO_2 and H_2O with oxygen vacancies in NiO (Figs. 5, 6b, d and 7). Finally, the left oxygen vacancies adsorb gaseous oxygen to form chemisorbed oxygen species and then combine with trapped electrons to regenerate O^{2-} of NiO [34]. Heating under irradiation does not change the path of reaction, but accelerates the decomposition rate of formates (Fig. 6d), and thus dramatically improves the activity in photothermal conditions (Fig. 2c and d).

4. Conclusions

A series of ZnO-CoNi catalysts were synthesized by oxalate-coprecipitation method and achieved excellent performance in photo-assisted TOM reaction. The microstructure of ZnO-CoNi catalyst is NiO nanocrystalline decorated on ZnO-CoNi solid solution determined by
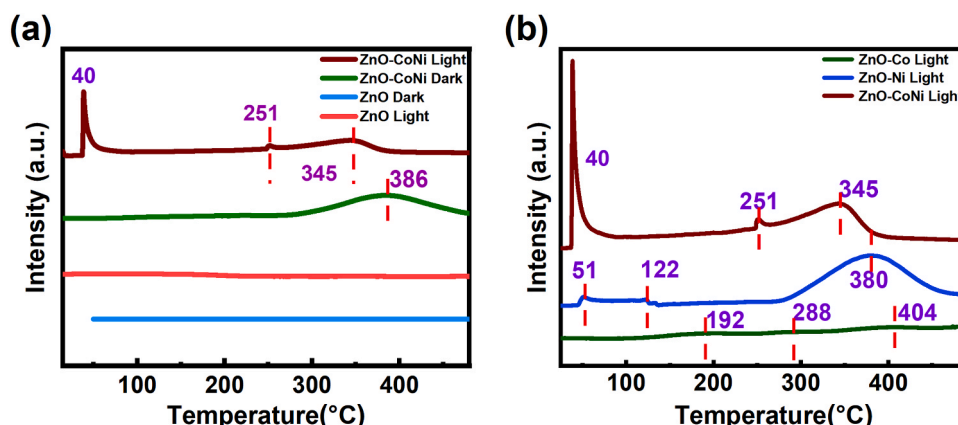

Fig. 7. In situ H_2-TPR spectra of (a)ZnO, ZnO-CoNi(9:6) and (b) ZnO-Co(11:4), ZnO-Ni(11:4).
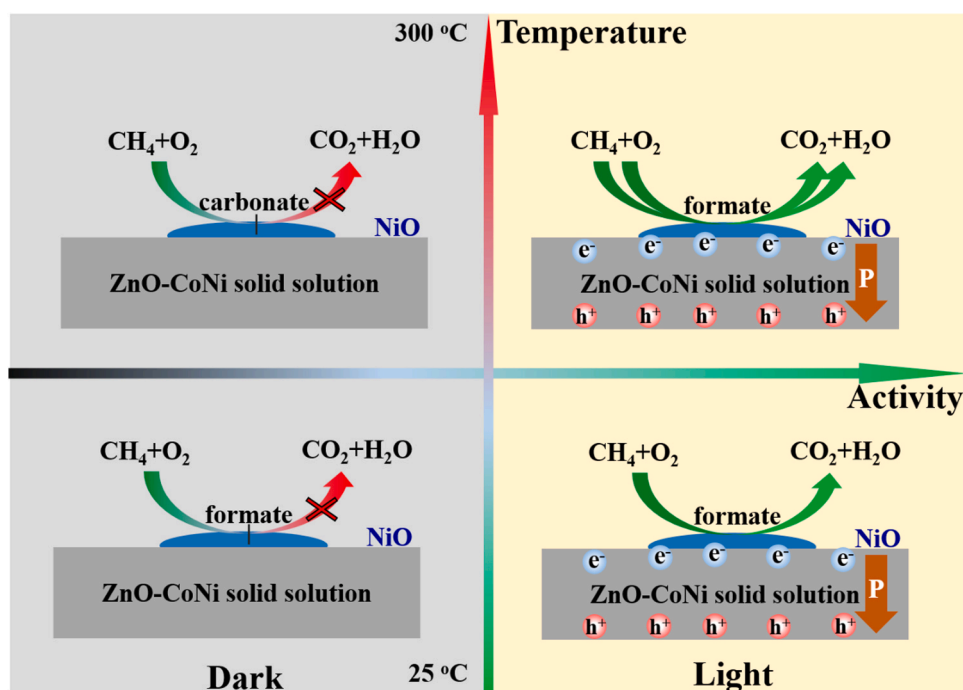
Fig. 8. Proposed reaction mechanisms of TOM on ZnO-CoNi catalyst in different conditions.

XRD, Raman and HAADF-STEM.

The in situ H_2-TPR characterizations demonstrate that segregated NiO nanocrystallines on ZnO-CoNi solid solution are the active sites for TOM reaction proceeding. Small amount of Co and/or Ni doping results in insufficient NiO active sites, while heavy doping leads to particle size growth of NiO (XRD). The optimized ZnO-CoNi(9:6) catalyst enables 88 % and 37 % photocatalytic conversion for 100 and 5000 ppm methane, respectively, under ambient conditions in a continuous reaction mode. It also exhibits good reaction and cycling stability without visible deactivation during 20 h test and repeatedly light turn off and on.

The UV-Vis, XPS, in situ DRIFT and in situ H_2-TPR characterizations demonstrate that Co doping is conducive to the formation of ZnO-CoNi solid solution with narrow band gap, plays a role in extending the utilization of the visible light and exciting more photogenerated electrons and holes. ZnO-CoNi with internal electric field provides a driving force for fast and spatially separation of photocarriers. NiO nanocrystallines supply low binding energy O^{2-} to oxidize CH_x species into CO_2 and H_2O. NiO nanocrystallines also can trap electrons to suppress the recombination of electrons and holes, and improve O^{2-} regeneration ability to promote the TOM reaction. The synergistic effect of ZnO-CoNi solid solution and NiO nanocrystalline dramatically promotes NiO/ZnO-CoNi photocatalytic activity for TOM reaction under ambient conditions.

The NiO/ZnO-CoNi catalyst with high activity and stability shows promising application in elimination large emission sources of methane and slow global warming. The unique structure of NiO/ZnO-CoNi catalyst may shed light on high efficiency catalysts development in photo and photothermal catalysis.

CRediT authorship contribution statement

Chen Sun: Investigation, Formal analysis, Data curation, Writing-original draft. **Kunfeng Zhao:** Conceptualization, Methodology, Formal analysis, Writing-review & Editing, Funding acquisition. **Adam Boies:** Writing-review & Editing, Validation. **Shuning Xiao:** Formal analysis, Conceptualization. **Zhiguo Yi:** Project administration, Funding acquisition, Resources, Writing-review & Editing, Supervision.

Declaration of Competing Interest

The authors declare that they have no known competing financial interests or personal relationships that could have appeared to influence the work reported in this paper.

Data Availability

Data will be made available on request.

Acknowledgements

Appendix A. Supporting information

Supplementary data associated with this article can be found in the online version at doi:10.1016/j.apcatb.2023.123124.

References

[1] P. Voosen, Ominous feedback loop may be accelerating methane emissions, Science 377 (2022) 250–251, https://doi.org/10.1126/science.add9091.

[2] S. Peng, X. Lin, R.L. Thompson, Y. Xi, G. Liu, D. Hauglustaine, X. Lan, B. Poulter, M. Ramonet, M. Saunois, Y. Yin, Z. Zhang, B. Zheng, P. Ciais, Wetland emission and atmospheric sink changes explain methane growth in 2020, Nature 612 (2022) 477–482, https://doi.org/10.1038/s41586-022-05447-w.

[3] G.H. Allen, Cause of the 2020 rise in atmospheric methane, Nature 612 (2022) 413–414, https://doi.org/10.1038/d41586-022-04352-6.

[4] M.A. Newton, A.J. Knorpp, V.L. Sushkevich, D. Palagin, J.A. van Bokhoven, Active sites and mechanisms in the direct conversion of methane to methanol using Cu in zeolitic hosts: a critical examination, Chem. Soc. Rev. 49 (2020) 1449–1486, https://doi.org/10.1039/c7cs00709d.

[5] M. Ravi, M. Ranocchiari, J.A. van Bokhoven, The direct catalytic oxidation of methane to methanol-a critical assessment, Angew. Chem. Int. Ed. 56 (2017) 16464–16483, https://doi.org/10.1002/anie.201702550.

[6] P. Schwach, X. Pan, X. Bao, Direct conversion of methane to value-added chemicals over heterogeneous catalysts: challenges and prospects, Chem. Rev. 117 (2017) 8497–8520, https://doi.org/10.1021/acs.chemrev.6b00715.

[7] G. Qi, T.E. Davies, A. Nasrallah, M.A. Sainna, A.G.R. Howe, R.J. Lewis, M. Quesne, C.R.A. Catlow, D.J. Willock, Q. He, D. Bethell, M.J. Howard, B.A. Murrer, B. Harrison, C.J. Kiely, X. Zhao, F. Deng, J. Xu, G.J. Hutchings, Au-ZSM-5 catalyses the selective oxidation of CH_4 to CH_3OH and CH_3COOH using O_2, Nat. Catal. 5 (2022) 45–54, https://doi.org/10.1038/s41929-021-00725-8.

[8] M. Zeng, L. Cheng, Q. Gu, B. Yang, B. Yu, J. Xu, Y. Zhang, C. Pan, X.M. Cao, Y. Lou, Y. Zhu, ZSM-5-confined Cr_1-O_4 active sites boost methane direct oxidation to C1 oxygenates under mild conditions, EES Catal. 1 (2023) 153–161, https://doi.org/10.1039/d2ey00080f.

[9] H. Song, X. Meng, Zj Wang, H. Liu, J. Ye, Solar-energy-mediated methane conversion, Joule 3 (2019) 1606–1636, https://doi.org/10.1016/j.joule.2019.06.023.

[10] X. Chen, Y. Li, X. Pan, D. Cortie, X. Huang, Z. Yi, Photocatalytic oxidation of methane over silver decorated zinc oxide nanocatalysts, Nat. Commun. 7 (2016) 12273, https://doi.org/10.1038/ncomms12273.

[11] C. Fu, F. Li, J. Yang, J. Xie, Y. Zhang, X. Sun, X. Zheng, Y. Liu, J. Zhu, J. Tang, X. Q. Gong, W. Huang, Spontaneous bulk-surface charge separation of TiO_2-{001} nanocrystals leads to high activity in photocatalytic methane combustion, ACS Catal. 12 (2022) 6457–6463, https://doi.org/10.1021/acscatal.2c01706.

[12] Z. Li, X. Pan, Z. Yi, Photocatalytic oxidation of methane over CuO-decorated ZnO nanocatalysts, J. Mater. Chem. A 7 (2019) 469–475, https://doi.org/10.1039/c8ta09592b.

[13] R. de Richter, T. Ming, P. Davies, W. Liu, S. Caillol, Removal of non-CO_2 greenhouse gases by large-scale atmospheric solar photocatalysis, Prog. Energy Combust. Sci. 60 (2017) 68–96, https://doi.org/10.1016/j.pecs.2017.01.001.

[14] W. Huang, A.C. Johnston-Peck, T. Wolter, W.C.D. Yang, L. Xu, J. Oh, B.A. Reeves, C. Zhou, M.E. Holtz, A.A. Herzing, A.M. Lindenberg, M. Mavrikakis, M. Cargnello, Steam-created grain boundaries for methane C-H activation in palladium catalysts, Science 373 (2021) 1518–1523, https://doi.org/10.1126/science.abj5291.

[15] D.J. Worth, M.E.J. Stettler, P. Dickinson, K. Hegarty, A.M. Boies, Characterization and evaluation of methane oxidation catalysts for dual-fuel diesel and natural gas engines, Emiss. Control Sci. Technol. 2 (2016) 204–214, https://doi.org/10.1007/s40825-016-0047-x.

[16] X. Feng, D. Liu, B. Yan, M. Shao, Z. Hao, G. Yuan, H. Yu, Y. Zhang, Highly active $PdO/Mn_3O_4/CeO_2$ nanocomposites supported on one dimensional halloysite nanotubes for photoassisted thermal catalytic methane combustion, Angew. Chem. Int. Ed. 60 (2021) 18552–18556, https://doi.org/10.1002/anie.202107226.

[17] L. Kang, X.Y. Liu, A. Wang, L. Li, Y. Ren, X. Li, X. Pan, Y. Li, X. Zong, H. Liu, A. I. Frenkel, T. Zhang, Photo-thermo catalytic oxidation over a TiO_2-WO_3-supported platinum catalyst, Angew. Chem. Int. Ed. 59 (2020) 12909–12916, https://doi.org/10.1002/anie.202001701.

[18] T. Cai, J. Yuan, L. Zhang, L. Yang, Q. Tong, M. Ge, B. Xiao, X. Zhang, K. Zhao, D. He, Ni-Co-O solid solution dispersed nanocrystalline Co_3O_4 as a highly active catalyst for low-temperature propane combustion, Catal. Sci. Technol. 8 (2018) 5416–5427, https://doi.org/10.1039/c8cy01062e.

[19] B. Xiao, K. Zhao, L. Zhang, T. Cai, X. Zhang, Z. Wang, J. Yuan, L. Yang, P. Gao, D. He, A green and facile synthesis of Co_3O_4 monolithic catalyst with enhanced total oxidation of propane performance, Catal. Commun. 116 (2018) 1–4, https://doi.org/10.1016/j.catcom.2018.07.013.

[20] J. Yang, W. Xiao, X. Chi, X. Lu, S. Hu, Z. Wu, W. Tang, Z. Ren, S. Wang, X. Yu, L. Zhang, A. Rusydi, J. Ding, Y. Guo, P.X. Gao, Solar-driven efficient methane catalytic oxidation over epitaxial $ZnO/La_{0.8}Sr_{0.2}CoO_3$ heterojunctions, Appl. Catal. B-Environ. 265 (2020), 118469, https://doi.org/10.1016/j.apcatb.2019.118469.

[21] R.D. Shannon, Revised effective ionic radii and systematic studies of interatomie distances in halides and chaleogenides, Acta Cryst. A 32 (1976) 751–767.

[22] D. Fischer, D. Zagorac, J.C. Schön, The presence of superoxide ions and related dioxygen species in zinc oxide-a structural characterization by in situ Raman spectroscopy, J. Raman Spectrosc. 53 (2022) 2137–2146, https://doi.org/10.1002/jrs.6441.

[23] J.B. Wang, H.M. Zhong, Z.F. Li, W. Lu, Raman study for E_2 phonon of ZnO in $Zn_{1-x}Mn_xO$ nanoparticles, J. Appl. Phys. 97 (2005), 086105, https://doi.org/10.1063/1.1865340.

[24] X.F. Wang, J.B. Xu, B. Zhang, H.G. Yu, J. Wang, X. Zhang, J.G. Yu, Q. Li, Signature of intrinsic high-temperature ferromagnetism in cobalt-doped zinc oxide nanocrystals, Adv. Mater. 18 (2006) 2476–2480, https://doi.org/10.1002/adma.200600396.

[25] T.L. Phan, R. Vincent, D. Cherns, N.X. Nghia, V.V. Ursaki, Raman scattering in Me-doped ZnO nanorods (Me = Mn, Co, Cu and Ni) prepared by thermal diffusion, Nanotechnology 19 (2008), 475702, https://doi.org/10.1088/0957-4484/19/47/475702.

[26] W. Fu, Y. Du, J. Jing, C. Fu, M. Zhou, Highly selective nitrate reduction to ammonia on CoO/Cu foam via constructing interfacial electric field to tune adsorption of reactants, Appl. Catal. B-Environ. 324 (2023), 122201, https://doi.org/10.1016/j.apcatb.2022.122201.

[27] L. Cao, D. Wang, R. Wang, NiO thin films grown directly on Cu foils by pulsed laser deposition as anode materials for lithium ion batteries, Mater. Lett. 132 (2014) 357–360, https://doi.org/10.1016/j.matlet.2014.06.114.

[28] J.L. Yang, Y.S. Lai, J.S. Chen, Effect of heat treatment on the properties of non-stoichiometric p-type nickel oxide films deposited by reactive sputtering, Thin Solid Films 488 (2005) 242–246, https://doi.org/10.1016/j.tsf.2005.04.061.

[29] M. Yang, H. Pu, Q. Zhou, Q. Zhang, Transparent p-type conducting K-doped NiO films deposited by pulsed plasma deposition, Thin Solid Films 520 (2012) 5884–5888, https://doi.org/10.1016/j.tsf.2012.05.005.

[30] W. Guo, H. Luo, D. Fang, Z. Jiang, J. Chi, W. Shangguan, In situ revealing the reconstruction behavior of monolayer rocksalt CoO nanosheet as water oxidation catalyst, J. Energy Chem. 70 (2022) 373–381, https://doi.org/10.1016/j.jechem.2022.02.049.

[31] D. Liu, D. Chen, N. Li, Q. Xu, H. Li, J. He, J. Lu, ZIF-67-derived 3D hollow mesoporous crystalline Co_3O_4 wrapped by 2D g-C_3N_4 nanosheets for photocatalytic removal of nitric oxide, Small 15 (2019), e1902291, https://doi.org/10.1002/smll.201902291.

[32] Y. Cao, L. Nyborg, U. Jelvestam, XPS calibration study of thin-film nickel silicides, Surf. Interface Anal. 41 (2009) 471–483, https://doi.org/10.1002/sia.3050.

[33] C.D. Wagner, W.M. Riggs, L.E. Davis, J.F. Moulder, G.E. Muilenberg, Handbook of X-ray photoelectron spectroscopy, Perkin-Elmer Corp. Minn. U. S. A. (1979) 82–84.

[34] K. Zhao, H. Tang, B. Qiao, L. Li, J. Wang, High activity of Au/γ-Fe_2O_3 for CO oxidation: effect of support crystal phase in catalyst design, ACS Catal. 5 (2015) 3528–3539, https://doi.org/10.1021/cs5020496.

[35] Z.Y. Zhang, T. Zhang, R.K. Wang, B. Yu, Z.Y. Tang, H.Y. Zheng, D. He, T. Xie, Z. Hu, Photo-enhanced dry reforming of methane over Pt-Au/P25 composite catalyst by coupling plasmonic effect, J. Catal. 413 (2022) 829–842, https://doi.org/10.1016/j.jcat.2022.07.028.

[36] Y. He, F. Guo, K.R. Yang, J.A. Heinlein, S.M. Bamonte, J.J. Fee, S. Hu, S.L. Suib, G. L. Haller, V.S. Batista, L.D. Pfefferle, In situ identification of reaction intermediates and mechanistic understandings of methane oxidation over hematite: a combined experimental and theoretical study, J. Am. Chem. Soc. 142 (2020) 17119–17130, https://doi.org/10.1021/jacs.0c07179.

[37] J. Deng, K. Bu, Y. Shen, X. Zhang, J. Zhang, K. Faungnawakij, D. Zhang, Cooperatively enhanced coking resistance via boron nitride coating over Ni-based catalysts for dry reforming of methane, Appl. Catal. B-Environ. 302 (2022), 120859, https://doi.org/10.1016/j.apcatb.2021.120859.